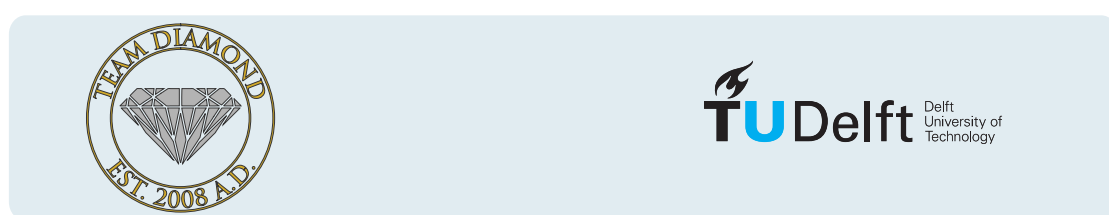


Parity Measurements on Weakly Coupled Carbon Spins in Diamond

MASTER OF SCIENCE THESIS
BY

Michiel Adriaan Rol



Supervisors:
Ir. J.CRAMER,
Dr. Ir. T.H.TAMINIAU,
Prof. Dr. Ir. B HANSON

Performed at:
Quantum Transport group
Kavli Institute of Nanoscience
Faculty of Applied Sciences, TU Delft

Abstract

Quantum error correction (QEC) is an essential ingredient for scaling up a quantum computer. The nitrogen-vacancy (NV) center in diamond is a promising candidate for such a scalable quantum computer. This thesis will first explain the tools available to control the NV-center and strongly coupled spins in its environment. We will then demonstrate how the spin register can be extended by addressing weakly coupled carbon-spins. The main result of this thesis is the creation of entanglement between two weakly coupled spins, for which initialization, control and read-out is required. We demonstrate entanglement with a fidelity of $F = 0.76 \pm 0.02$, well above the quantum limit for an entangled state. The last chapter will provide an outlook on how the capabilities developed can be extended to implement QEC.

Contents

1	Introduction	5
1.1	Quantum Error Correction	5
1.2	The Nitrogen Vacancy Center in Diamond	6
1.3	Goal of the project	6
2	The Nitrogen-Vacancy center in Diamond	9
2.1	The electronic spin	9
2.1.1	Initialization and readout of the electronic-spin state	9
2.1.2	Controlling the electronic-spin state	10
2.2	Controlling nuclear spins	10
2.2.1	The Hyperfine Interaction	10
2.2.2	Controlling the nitrogen nuclear spin	11
2.2.3	Hyperfine coupling of carbon-13 spins	11
2.2.4	Weakly versus strongly coupled carbon spins	12
2.3	Decoherence	12
2.3.1	Decoherence time	13
2.3.2	Relation between decoherence and transition broadening	13
3	Addressing Weakly-coupled Carbon Spins	15
3.1	Extending Electron Coherence	15
3.1.1	Spin-Echo	15
3.1.2	Dynamical Decoupling	16
3.2	Identifying weakly-coupled carbon-spins	16
3.2.1	Dynamical decoupling spectroscopy	16
3.2.2	The effect of dynamical decoupling on nuclear spins	17
3.2.3	Identifying Individual Carbon-spins	18
3.3	Characterizing weakly-coupled carbon spins	19
3.3.1	Basic operations	19
3.3.2	Carbon Ramsey experiment	20
4	Entangling Weakly-coupled Carbon Spins	23
4.1	Initialization and readout of single spins	23
4.2	Parity measurements	24
4.3	Quantum state tomography	25
4.3.1	Readout	25
4.3.2	Initialization and tomography of multiple weakly coupled spins	25
4.4	Demonstrating entanglement between weakly coupled carbons	25
5	Towards Quantum Error Correction	29
5.1	Deterministic Parity Measurements	29
5.2	Multi Qubit Control	29
5.2.1	Overview of the simulations	29

5.2.2	Results of the simulation	30
A	Dynamical Decoupling Spectroscopy	37
A.1	Mathematical description of dynamical decoupling spectroscopy	37
A.2	Fingerprint analysis	37
B	Constants and Experimental values	39

1

Introduction

Although computers have increasingly become part of daily life they fall short when confronted with difficult problems such as protein folding or searching a large unsorted database. Quantum computers promise an exponential speedup for certain classes of problems making it possible to solve these problems on a human timescale.

The idea of using a quantum mechanical system to simulate physics was first explored by Feynman[8]. Because the number of operations required to simulate a quantum system scales exponentially with the number of particles in the system it is not feasible to classically simulate such a system. By manipulating a quantum mechanical system directly this scaling problem can be circumvented.

It was the idea of quantum simulation that led to the idea of exploiting quantum effects to perform computations. Shor's algorithm [23] is a prime example of how the advantageous scaling of quantum systems can be exploited to perform more efficient computations.

Shor's algorithm is an algorithm for prime factorization, where the best known classical algorithms for prime factorization scale exponentially Shor's algorithm scales polynomially. Because of the speedup provided by Shor's and other quantum algorithms it is possible to solve classes of problems that were previously unsolvable, such as the breaking of RSA encryption that relies on prime factorization being a computationally hard problem. Shor's algorithm has been shown to work on a small scale quantum computer [28]. However to take full advantage of the efficient scaling behaviour of quantum computations a scalable quantum computer is required.

1.1 Quantum Error Correction

One of the main challenges in creating a scalable quantum computer is the effect of errors. Because a quantum computer uses entanglement between multiple qubits as a resource an error on a single qubit can quickly propagate through the system. Using quantum error correction (QEC) it is possible to correct for such errors. The threshold theorem states the final error probability of a quantum algorithm on a large register can be made arbitrarily small, if the probability of an error on a single qubit is below a certain threshold and QEC is applied [14]. This makes quantum error correction a stepping stone on the way to realizing a scalable quantum computer [17].

Experiments demonstrating a form of QEC have been demonstrated in a range of systems. Codes correcting for one type of quantum error have been implemented with nuclear magnetic resonance [5, 15], trapped ions [22] and superconducting qubits [20]. Recently two groups have implemented three qubit gate based QEC using the nitrogen-vacancy (NV) center in diamond [26, 29].

Although schemes exist to implement a scalable quantum computer using a purely gate based architecture most approaches rely on correcting for quantum errors by performing repeated parity measurements. An example of such an approach is surface coding [9]. For this reason the present work will focus on performing the parity measurements required for such error correcting schemes.

QEC is similar to classical error correction through majority voting. In classical majority voting a single bit is encoded onto a *logical* bit consisting of multiple regular bits. When an error on a bit has occurred the original bit can be recovered by measuring all the individual bits and determining the original state by majority voting.

In QEC the quantum bit (qubit) is encoded onto a logical qubit consisting of multiple regular qubits. A consequence of classical majority voting is that it destroys a quantum state because it

requires all bits to be measured. By measuring the parity of two qubits the difference between two states can be determined without measuring the individual states. If two states are parallel in the parity basis the parity measurement will return a positive result, if they are anti-parallel a negative result. Performing a parity measurement on multiple qubits allows quantum errors, such as a bit-flip, a phase-flip or the combination of both, to be diagnosed.

Figure 1.1 shows a circuit diagram for three qubit measurement based QEC. The state $|\psi\rangle_{C2}$ is encoded onto a logical qubit consisting of qubits C1, C2 and C3. A parity measurement is performed on qubits C1 and C2, and on C2 and C3, by reading out an ancilla qubit e . From the result of the parity measurements it can be determined on which qubit an error occurred. Based on this result the error can be corrected. Because the logical qubit does not need to be decoded to correct for the error it is possible to repeat the error correcting part of the circuit, thereby improving the protection of the qubit. The original qubit can be recovered by decoding the logical qubit.

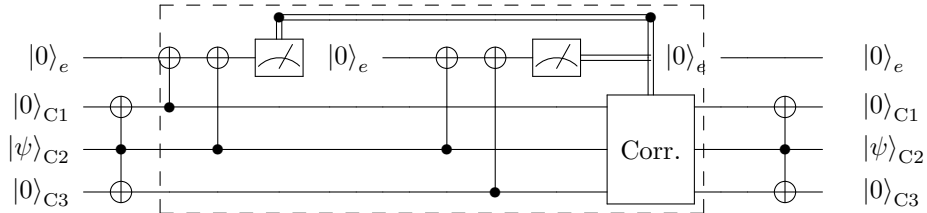


Figure 1.1 – Gate circuit for three qubit error correction. First the state of $C2$ is encoded onto three qubits. To diagnose an error an ancilla qubit is used to perform two parity measurements on the encoded qubits. The result of these measurements is used to determine what gates to apply to correct for the error if it occurred. These error correcting operations (in the dashed lines) can be repeated to continuously protect the encoded qubits against quantum errors. The three qubit error correction code can correct for one type of quantum error.

In order to implement measurement based error correction as depicted in Fig. 1.1 we require initialization and control over three qubits and an ancilla that can be used to read out the main qubits. Furthermore we need to be able to perform parity measurements on these qubits and deterministically perform operations based on the outcome of these parity measurements to correct for errors.

1.2 The Nitrogen Vacancy Center in Diamond

The NV-center is a promising candidate for quantum computation [4]. The NV-center is a naturally occurring impurity in diamond of which the electronic spin can be optically addressed and read out. By applying microwave pulses to the NV-center it is possible to control and initialize strongly coupled spins in its environment [21]. This spin register can be extended by addressing weakly coupled spins [26, 29].

Because of optical interface of the NV-center it is possible to link physically independent NV-centers together [3]. This has been used to demonstrate quantum teleportation [19].

This unique combination of a local qubit register with an optical interface makes the NV-center a suitable system to implement a node based design for a scalable quantum computer[16].

1.3 Goal of the project

In order to realize QEC at least three qubits are required to correct for a single type of error and more than five qubits are required to correct for a universal error. Because the probability of finding enough strongly coupled carbons to implement QEC is small and goes down rapidly the more spins are required [26, 29] we address weakly coupled spins using the methods developed by Taminiau et al. [26].

The goal of this project is to implement a parity measurement and demonstrate entanglement created by this parity measurement using weakly coupled spins in the environment of the NV-center. The parity measurement is required for QEC in particular and measurement based approaches to quantum information in general. This is done in a measurement environment that is designed from start to be compatible with the feed forward operations required for QEC.

The next chapter will explain the tools available to control the NV-center and strongly coupled spins. Chapter 3 will discuss how coherence can be extended in order to control weakly coupled

carbons. In Chapter 4 these techniques are used to first initialize multiple weakly coupled carbon spins before creating entanglement using the parity measurement. The last chapter will provide an outlook on how the capabilities developed can be extended to perform deterministic parity measurements and show simulations indicating that it is possible to perform multi qubit error correction using weakly coupled spins.

2

The Nitrogen-Vacancy center in Diamond

The nitrogen-vacancy (NV) center in diamond provides a natural occurring qubit register in a solid state environment. This chapter will explain how the electronic spin can be initialized, controlled and read-out using optical and microwave pulses. The electronic spin can be used to initialize control and readout nuclear spins in the environment trough the hyperfine interaction. It is shown how the coherence of the electron poses challenges to directly control the nuclear spin. The next chapter will demonstrate how to extend the electron coherence so that more spins can be controlled.

2.1 The electronic spin

The NV-center is a naturally occurring impurity in diamond consisting of a substitutional nitrogen and an adjacent lattice vacancy (Fig. 2.1a). The NV-center can be in a neutral charge state (NV^0) or in a negatively charged state (NV^-). In this thesis we are mainly interested in the negatively charged state, where an additional electron is captured from the environment. For the NV^- the ground state is a spin-triplet that forms the basis of our qubit.

The electronic ground state can be described by the Hamiltonian [2]:

$$H_{\text{GS}} = \Delta S_z^2 + \gamma_e \mathbf{B} \cdot \mathbf{S} \quad (2.1)$$

Where S_i are the Pauli-spin operators, $\gamma_e = 2.802 \text{ MHz/G}$ is the electron gyro-magnetic ratio and $\Delta \approx 2.88 \text{ GHz}$ is the zero-field splitting. In this expression the interactions with the nitrogen nucleus and the carbon spin bath are not included. In the experiments a magnetic field $B_z = 304 \text{ G}$ is applied along the NV-axis¹. The magnetic field lifts the degeneracy of the $m_s = \pm 1$ so that we can define our electronic qubit as the two level system $m_s = 0 := |0\rangle$ and $m_s = +1 := |1\rangle$.

2.1.1 Initialization and readout of the electronic-spin state

The transitions between the electronic ground-state and excited state are spin dependent and lie in the optical domain ($\sim 637 \text{ nm}$). At low temperatures these transitions can be resonantly excited. For this reason, experiments were performed at cryogenic temperatures (4 K). The exact frequencies of these transitions depend on magnetic field and strain [12].

Figure 2.1b shows the optical transitions used to initialize and read-out the electronic spin. The E' transition excites both the $m_s = +1$ and the $m_s = -1$ states to the excited state. The E_x transition excites the $m_s = 0$ state to the excited state. There is a small probability that the spin is flipped in an optical cycle, denoted by the dashed line.

By cycling an optical transition the spin state can be read-out and initialized [21]. By applying a pulse to the E_x transition a photon can be detected when the state falls back to the ground state. Because the E_x only excites the $m_s = 0$ state photons can only be detected when the system is in the $|0\rangle$ -state.

By pumping one of these transitions the spin can be initialized. Pumping will cause the population to cycle between the ground and excited state with a small probability of the spin flipping. When the spin flips it ends up in the state that is not being excited and stays there.

¹The NV-axis is the axis going trough both the nitrogen and the vacancy.

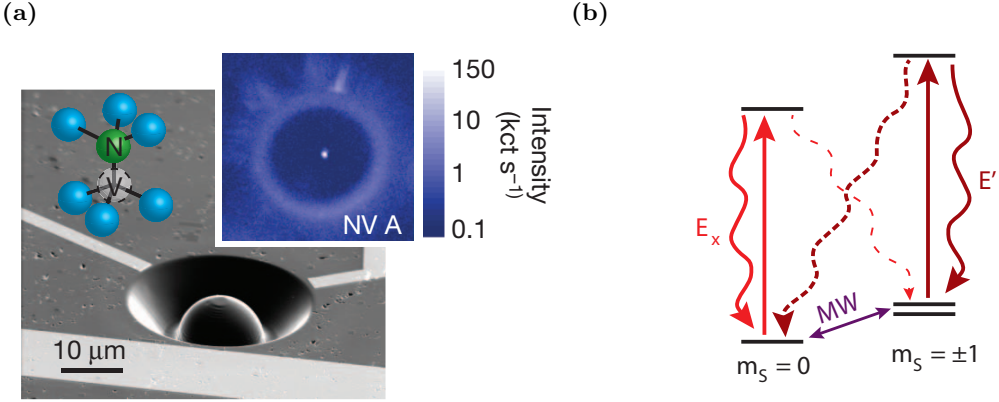


Figure 2.1 – (a) Scanning electron microscope image of a diamond sample with solid immersion lens (SIL) similar to that used in the experiments. A gold stripline, visible as the white area below the SIL is used to apply microwave pulses. Overlaid sketch shows a schematic representation of the NV-center. Inset shows a confocal microscope image of the NV-center in the center of the SIL. (b), Energy levels used for initialization and readout of the electronic-spin state. Figures adapted from Robledo et al. [21]

Because the number of pumping cycles before the spin flips is limited, the fidelity with which the spin can be read-out is limited by the detection efficiency of the emitted photons. A solid immersion lens (SIL), visible in Fig. 2.1a, is milled onto the sample to maximize the detection efficiency. The experiments in this thesis were performed at a readout fidelity of $F \approx 91\%$.

2.1.2 Controlling the electronic-spin state

The state of a qubit can be represented as a vector on the Bloch-sphere where the $|0\rangle$ -state lies at the north pole and the $|1\rangle$ -state at the south pole. The state vector rotates around the quantization-axis with a frequency depending on the energy splitting between the two states: the Larmor frequency. For the NV-electronic spin the quantization axis points in the z-direction (towards $|0\rangle$) and the Larmor frequency is given by:

$$\omega_L = \Delta + \gamma_e B_z \quad (2.2)$$

By applying an external field a term is added to the Hamiltonian, the quantization-axis is changed, thereby changing its evolution. By applying microwaves with a frequency equal to ω_L the transition between $|0\rangle$ and $|1\rangle$ can be driven [13]. Resonant microwave pulses are applied to the sample through an on-chip stripline (Fig. 2.1a).

2.2 Controlling nuclear spins

The electronic-spin interacts with each nuclear spins in its environment through the hyperfine interaction, which is dependent on their position. Dependent on the strength of the hyperfine interaction close by spins can be controlled directly by applying microwave pulses.

2.2.1 The Hyperfine Interaction

The coupling between the electronic spin of the NV-center and a nuclear-spin is given by the hyperfine-interaction. The hyperfine interaction is a spin-spin interaction.

For nuclear spins the Hamiltonian therefore depends on the electronic spin-state of the NV-center. For a magnetic field (B_z) in the z-direction the Hamiltonian is given by:

$$H_0 = -QI_z^2 + \gamma_n B_z I_z \quad (2.3)$$

$$H_1 = -QI_z^2 + \gamma_n B_z I_z + H_{HF} \quad (2.4)$$

Corresponding respectively to the electronic spin being in the $m_s = 0$ and in the $m_s = +1$ state. Where I and S are the nuclear and electronic spin operators, γ_n is the gyro-magnetic ratio of the nucleus and Q is the nuclear quadrupole splitting. The quadrupole term is $Q = 2\pi \cdot 4.946$ MHz for the nitrogen-14 spin [2]. And $Q = 0$ for carbon-13 spins.

The Larmor frequency for a nucleus is given by Eq. (2.5):

$$\omega_L = -QI_z^2 + \gamma_n B_z \quad (2.5)$$

2.2.2 Controlling the nitrogen nuclear spin

To obtain high-fidelity electron spin control it is desirable to initialize the nitrogen of the NV-center. In this work this is done through measurement based initialization (MBI) using the hyperfine interaction.

Because both the zero-field splitting Δ of the electronic-spin is much larger than the hyperfine coupling between the nuclear and electronic spin, the secular approximation can be used, leading to the following system Hamiltonian:

$$H_{\text{GS}} = \Delta S_z^2 + \gamma_e \mathbf{B} \cdot \mathbf{S} - Q I_z^2 + \gamma_n B_z I_z - A_N S_z \cdot I_z \quad (2.6)$$

Where $A_N = 2\pi \cdot 2.186$ MHz. The hyperfine interaction between the nitrogen and electronic spin causes the transition between $m_s = 0$ and $m_s = 1$ to be split. This magnitude of the splitting is equal to A_N and is clearly resolved in the Electron Spin Resonance (ESR) shown in the top panel of Fig. 2.2.

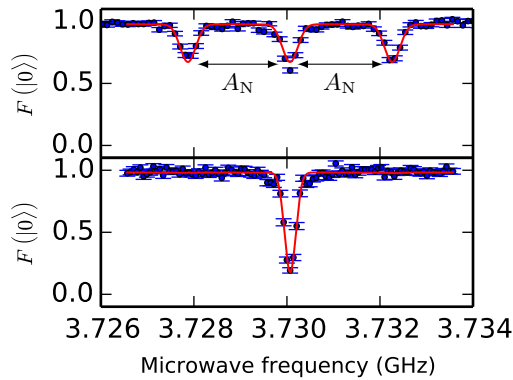


Figure 2.2 – Electron Spin Resonance (ESR) for uninitialized (top) and initialized nitrogen spin (bottom) of the $m_s = 0 \rightarrow m_s = +1$ transition. In the ESR the spin is prepared in $|0\rangle$, a microwave pulse is applied and finally the electron spin fidelity with $|0\rangle$, $F(|0\rangle)$ is measured. The microwave frequency is swept. When the microwave is on resonance the spin will be rotated out of $|0\rangle$ and a decrease will be visible in the signal. In the top figure the transition is split due to the interaction with the NV’s nitrogen nuclear spin. In the lower figure the nitrogen spin state is initialized and the splitting disappears.

The hyperfine interaction can be used to measure the nitrogen’s spin state. Every time an experiment is started the nitrogen starts out in a mixed state. This means that every time an uninitialized nitrogen is measured it is equally likely to end up in one of its three states, as can be seen in the top panel of Fig. 2.2. The nitrogen state can be measured by initializing the electron in the split $m_s = +1$ state and driving one of the transitions to $m_s = 0$, factually implementing a controlled-NOT gate. Only if the nitrogen was in the state corresponding to the transition being driven will a measurement of the $m_s = 0$ state give a positive result.

By resetting and repeating this procedure until a positive result is measured the nitrogen-spin can be initialized. The electronic spin-state can be reset by applying a resonant laser as shown in the previous section. The nuclear spin-state can be reset by applying two resonant lasers resonant with E_x and E' to introduce electron-nuclear flip-flops.

This procedure is known as measurement based initialization (MBI) and is used in our experiments. The lower panel of Fig. 2.2 shows an ESR after the nitrogen has been initialized using MBI.

2.2.3 Hyperfine coupling of carbon-13 spins

For carbon-13 spins the hyperfine term (H_{HF}) of Eq. (2.4) consists of a contact term and a dipole term. The contact term results from an overlap between the electronic- and nuclear- wave-functions. The contact term is negligible for all but the carbon-spins closest to the NV-center. For close-by carbon spins hyperfine couplings have been calculated [10, 11] and measured [24].

For carbons where the contact term is negligible the dipole term is dominant and is given by [6]:

$$H_{\text{dip}} = \frac{\mu_0 \gamma_e \gamma_C \hbar^2}{4\pi r^3} [\mathbf{S} \cdot \mathbf{I} - 3(\mathbf{S} \cdot \hat{\mathbf{n}}_{\text{HF}})(\mathbf{I} \cdot \hat{\mathbf{n}}_{\text{HF}})] \quad (2.7)$$

Where \hat{n}_{HF} is a unit vector pointing from the electronic spin to the nucleus, r is the distance between the electronic and nuclear spin, and μ_0 the magnetic constant. The dipole term can be split into a parallel (A_{\parallel}) and orthogonal (A_{\perp}) component such that:

$$H_{\text{HF}} = A_{\parallel} I_z + A_{\perp} I_x \quad (2.8)$$

From Eq. (2.7) the parallel and orthogonal components of the hyperfine interaction, with respect to the NV-axis along the z-direction, can be derived to be:

$$A_{\parallel} = -\frac{\mu_0 \gamma_e \gamma_C \hbar^2}{4\pi r^3} \left(3 \cdot \frac{z^2}{r^2} - 1 \right) \quad (2.9)$$

$$A_{\perp} = -\frac{\mu_0 \gamma_e \gamma_C \hbar^2}{4\pi r^3} \left(3 \cdot \frac{\sqrt{x^2 + y^2} \cdot z}{r^2} \right) \quad (2.10)$$

2.2.4 Weakly versus strongly coupled carbon spins

Carbon spins can be controlled using the methods described in Section 2.2.2 when it is possible to selectively address its spin-dependent transitions. When two transitions can be resolved in an ESR they can be addressed by applying microwave pulses of the corresponding frequencies. However if two transitions overlap in an ESR, applying a microwave pulse at the corresponding frequency will address both transitions.

Two transitions cannot be resolved when the splitting between them is smaller than the width of the transition. The magnitude of the splitting is determined by the strength of the interaction and the broadening of the transitions is caused by decoherence. We define a spin to be strongly coupled when it is possible to readily resolve its transitions in an ESR experiment with negligible power broadening. Conversely a spin is weakly coupled when it is not possible to readily resolve its transitions in an ESR. Figure 2.3 shows a schematic overview of the different coupling regimes.

As the presence of strongly coupled carbons close to the NV-center is governed by probability and the probability of getting 3-5 strongly coupled carbons is very low it is necessary to develop methods to address weakly coupled carbons. The next chapter will demonstrate methods to extend the coherence time and address weakly coupled carbons, thereby enlarging the spin-register.

Before coherence can be extended to control weakly coupled spins it is necessary to understand what decoherence is and how it relates to the broadening of transitions. The next section will explain decoherence and give an estimation for the hyperfine strength above which a spin is strongly coupled.

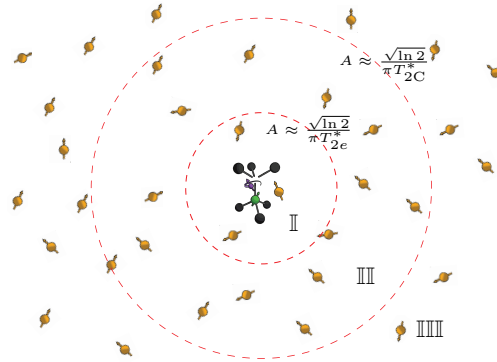


Figure 2.3 – Schematic representation of different coupling regimes. Carbons in region I are in the strong coupling regime, transitions of these spins can be readily resolved and they can be controlled using the methods described in Section 2.2.2. In the weak coupling regime (region III) carbon-spins are coupled more strongly to the NV-center than to the spin-bath but not strong enough to be readily resolvable in an ESR. Some of these spins can be controlled through dynamical decoupling [25]. In the very-weak coupling regime (region IIII) the coupling to the spin-bath is stronger than the coupling to the NV-center. These spins cannot presently be addressed.

2.3 Decoherence

Whether a nuclear spin is weak or strongly coupled is set by the coherence time of the electron spin. This section will explain decoherence as well as give an estimation for when a carbon spin is

strongly coupled.

An ESR signal is broadened because the NV-center interacts with the spin bath in its environment. The spin bath consists of spins that are coupled to the NV-center. Just like the uninitialized nitrogen spin these are in a mixed state. This means that for every iteration of an experiment the spin bath can have a different configuration. These different configurations of the spin bath slightly shift the addressed electron transition causing the broadening of the transition.

2.3.1 Decoherence time

The variations in the spin-bath configuration can be measured with a Ramsey experiment. In a Ramsey experiment (Fig. 2.4a) the electronic spin is brought into a superposition between the $|0\rangle$ and $|1\rangle$ -state where it freely evolves for a time τ . Provided the coherent superposition is preserved, a final pulse brings the state back into $|0\rangle$ where it is read out.

By applying a slight detuning to the rotating frame used to keep the phase fixed an oscillation can be seen in the signal (Fig. 2.4b). Due to the different spin-bath configurations the evolution frequency varies slightly between experiments, this causes the measured signal to decay as the different oscillations move out of phase with each other. The decay is known as decoherence and the $1/e$ -time of the decay is the decoherence time T_2^* . For a Ramsey experiment the decay follows a Gaussian profile:

$$F(|0\rangle)(\tau) = e^{-(\frac{\tau}{T_2^*})^n} \quad (2.11)$$

Where $n = 2$ for a Gaussian profile. The T_2^* of the NV-electron spin used in this thesis was measured to be $T_{2,e}^* = 4.54 \pm 14 \mu\text{s}$ with initialized nitrogen-spin. The decay is consistent with a Gaussian profile: $n = 1.81 \pm 0.14$.

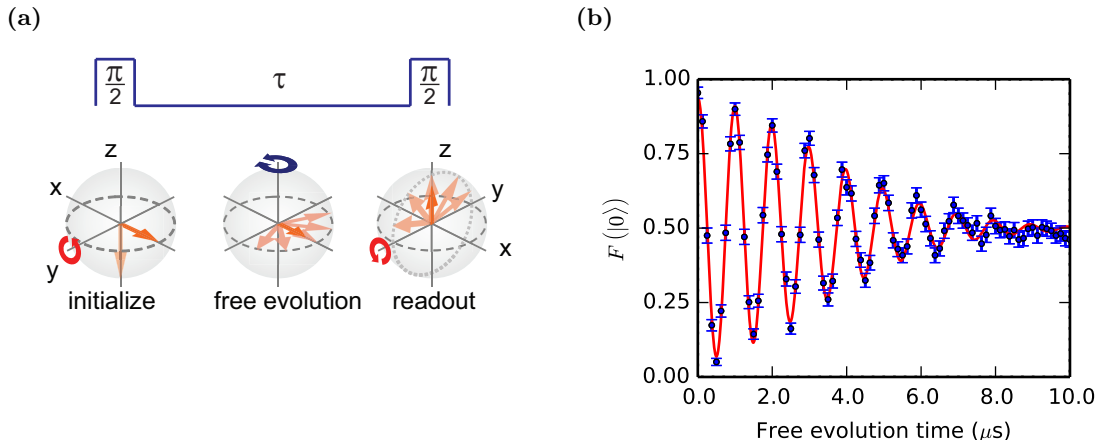


Figure 2.4 – (a) schematic representation of a Ramsey experiment. Figure from de Lange [6]. In a Ramsey experiment a qubit is brought into the xy -plane by a $\pi/2$ -pulse where it evolves freely for a time τ before being subjected to a final $\pi/2$ pulse to read out its x -component. By applying a detuning (ω_d) to the rotating frame the spin will pick up a phase $\phi = \omega_d\tau$ during free evolution. The final pulse will rotate the spin towards the poles depending on the phase picked up during free evolution. This manifests itself as an oscillation. Because the configuration of the spin-bath is slightly different between experiments the frequency of the oscillation will vary with each iteration. This variation in frequency between iterations will cause the oscillation to decay. (b) Ramsey experiment for the electronic spin. The y -axis shows the fidelity ($F(|0\rangle)$) of the measured state to the $|0\rangle$ -state of the electronic spin. A $T_{2,e}^*$ of $4.54 \pm 0.14 \mu\text{s}$ was measured for the electronic spin. The decay follows a Gaussian profile within uncertainty $n = 1.81 \pm 0.14$.

2.3.2 Relation between decoherence and transition broadening

The decay in a Ramsey experiment is a measure for variations of the spin-bath in the time-domain while the broadening of transitions in an ESR is a measure for variations of the spin-bath in the frequency domain. The decay of the Ramsey and the shape of the ESR for negligible power broadening are related through a Fourier transform and described by:

$$\mathcal{F}\{K(\tau)\} = Ce^{-\frac{(2\pi \cdot f)^2 \cdot T_{2e}^{*2}}{4}} \quad (2.12)$$

Where C is a normalization constant. Because the decay of the Ramsey is Gaussian the shape of a transition in the ESR is also Gaussian.

Two identical Gaussians can be readily resolved when the separation between their maxima is larger than their full-width-half-maximum (FWHM). The FWHM (in Hz) of the ESR is given by Eq. (2.13):

$$\text{FWHM} = \frac{2\sqrt{\ln 2}}{\pi T_{2e}^*} \quad (2.13)$$

An estimation of when carbon spins can be resolved is given by the strength of the hyperfine interaction. At low magnetic field ($\gamma_e B \ll A$) the splitting caused by a carbon spin is equal to the total interaction strength A . At high field ($\gamma_e B \gg A$) the secular approximation is valid and the splitting is equal to the parallel component of the hyperfine A_{\parallel} . We can readily resolve a transition when the shift due to the corresponding interaction is larger than the FWHM of the transition.

At a natural concentration of carbon-13 spins ($\mu = 1.1\%$) NV-centers have a typical electron $T_{2e}^* \approx 2 \mu\text{s}$ at low field that depends on the exact configuration of the spin-environment. Increasing the carbon-13 concentration generally reduces T_{2e}^* . On the sample used for the experiments $T_{2e}^* = 4.54 \pm 0.14 \mu\text{s}$ was measured at 304 G. This means that the hyperfine coupling must be larger than $2\pi \cdot 265 \text{ kHz}$ in a typical NV-center, and larger than $2\pi \cdot 117 \text{ kHz}$ in the sample used in this thesis for a carbon to be strongly coupled.

3

Addressing Weakly-coupled Carbon Spins

In order to realize quantum error correction at least three qubits and at least five to correct for a universal error will be needed. Strongly coupled carbon spins can be controlled as explained in the previous chapter [21, 29]. However the probability of finding enough of these spins to implement QEC is very small. The probability of finding three or more strongly coupled carbons spins in an NV-center is low and goes down the more carbons are required [26, 29]. Additionally strongly coupled nuclear spins are prone to decohere when the electronic spin is optically addressed[18]. A problematic feature for QEC which relies on repeatedly measuring errors to be able to correct for them.

By addressing weakly coupled carbon spins the spin register can be enlarged with spins that are not affected as strongly by the readout of the electron spin. However to address weakly coupled carbon spins the coherence of the electron needs to be extended. This is done trough dynamical decoupling [7]. Van der Sar et al. [27] have demonstrated how to integrate gates on the nitrogen spin with dynamical decoupling sequences. To address these weakly coupled carbon spins we use the dynamical decoupling sequence used to extend the coherence [25]. In the next chapter it is demonstrated how this control is used to perform parity measurements and create entanglement.

In this chapter it will first be explained how the coherence can be extended trough dynamical decoupling so that weakly coupled carbon spins can be addressed. The dynamical decoupling sequence will then be used to identify spins in the environment. These spins are characterized so that they can be controlled in the next chapter.

3.1 Extending Electron Coherence

To be able to resolve weakly coupled carbons it is necessary to extend the coherence of the electron spin. By using a spin-echo the effect of variations in the environment *between* experiments can be eliminated, making variations of the spin-bath *during* a single sequence (between $\pi/2$ pulses) the main source of decoherence. By dynamical decoupling the effect of these nuclear spin-spin dynamics on the coherence can be minimized and the interactions with the spin-bath can be exposed.

3.1.1 Spin-Echo

A spin echo experiment (Fig. 3.1) is very similar to a Ramsey experiment. The difference is an additional π pulse that is added in the middle of the experiment exactly between the $\pi/2$ pulses of the Ramsey sequence. In a spin echo the state is brought into the xy -plane where it evolves for a time $\tau/2$ before a π -pulse, along the y -direction in the rotating frame, is applied. It evolves for another $\tau/2$ before a final $\pi/2$ -pulse ideally rotates it back towards $|0\rangle$ and it is read out.

The key component of a spin-echo is the central π -pulse that cancels out the effect of quasi-static variations in the spin-bath configuration. The π -pulse can be seen as turning the reference frame of the NV-spin upside down. If the spin-bath configuration is approximately static during the sequence, the detuning of the evolution frequency with respect to the central frequency during the first part will be exactly opposite to the detuning during the second part. This means that any phase difference picked up during the first half of the evolution is canceled out during the second half of the evolution.

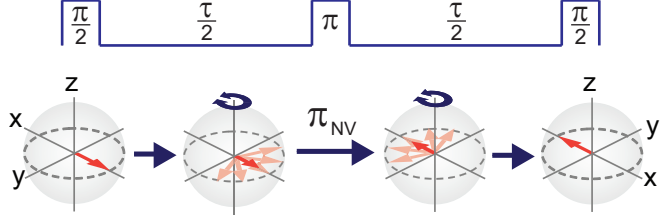


Figure 3.1 – In a spin echo experiment the qubit is brought into the xy -plane of the Bloch-sphere by a $\pi/2$ -pulse. Here it freely evolves for a time $\tau/2$ before being flipped by a π -pulse along the y -axis of the rotating frame. It is let to evolve for another $\tau/2$ before a final $\pi/2$ pulse brings is used to read out the x -component. If the spin-bath configuration does not change during the free evolution time τ the state vector will end up along the x -axis irrespective of the initial spin-bath configuration. Figure from de Lange [6].

Due to nuclear spin-spin interactions the spin-bath does not remain static during experiments and the cancellation is not perfect, some phase is picked up causing the signal to ultimately decohere. This coherence time (T_2) is defined as the $1/e$ value of the decay of a spin echo experiment and measures decoherence due to dynamics in the spin-bath during an experiment. T_2 was measured to be 1.10 ± 0.01 ms.

3.1.2 Dynamical Decoupling

A natural way to extend the phase cancellation properties of the spin-echo experiment to shorter timescales is by applying more π -pulses. This procedure is known as dynamical decoupling. Similar to how the spin-echo cancels out phase picked up due to any variations that are quasi-static on the time-scale of the experiment, dynamical decoupling cancels out phase due to variations on the time-scale of the π -pulses. Dynamical decoupling can significantly improve coherence times [7].

On the NV-center used in this thesis a coherent signal¹ is measured after more than 40 ms for 256 pulses. Work on ensembles indicates that that this can be improved even further by applying more pulses: a coherence time of $T_{DD} \approx 0.6$ s was reported at 77 K [1].

3.2 Identifying weakly-coupled carbon-pins

When discussing the Ramsey and the spin-echo experiment we have treated the NV-center as being affected by the spin-bath but not affecting it. In reality the interaction works both ways and the NV-spin does affect the nuclear spins. It is possible to probe these interactions using a dynamical decoupling spectroscopy. A dynamical decoupling spectroscopy provides a type of fingerprint of the nuclear spin environment from which the the hyperfine interaction for the individual spins can be determined [25, 26].

This section will discuss the effect of dynamical decoupling on the electron-nucleus dynamics. This is used to explain the features in the fingerprint of Fig. 3.2 and identify several individual nuclear spins.

3.2.1 Dynamical decoupling spectroscopy

In a dynamical decoupling spectroscopy experiment the electron is prepared in the $|X\rangle = \frac{1}{\sqrt{2}}(|0\rangle + |1\rangle)$ state. It is subjected to a pulse sequence consisting of $N/2$ blocks of the form $\tau - \pi - 2\tau - \pi - \tau$, where τ is a wait time and π a π -pulse. The experiment is concluded by measuring $\langle X \rangle$. The fingerprint is the result of many repetitions for a range of inter-pulse delays 2τ .

Part of a dynamical decoupling spectroscopy result can be seen in Fig. 3.2. When the electron spin performs an entangling operation on a spin in the environment coherence is lost when the electron spin is measured. In a dynamical decoupling spectroscopy such an interaction is visible as a decrease in the expectation value $\langle X \rangle$.

A broad collapse of the signal is clearly visible around $\tau/(4\tau_L) = m$ for odd m . This broad collapse is caused by the electron performing an entangling gate on multiple spins.

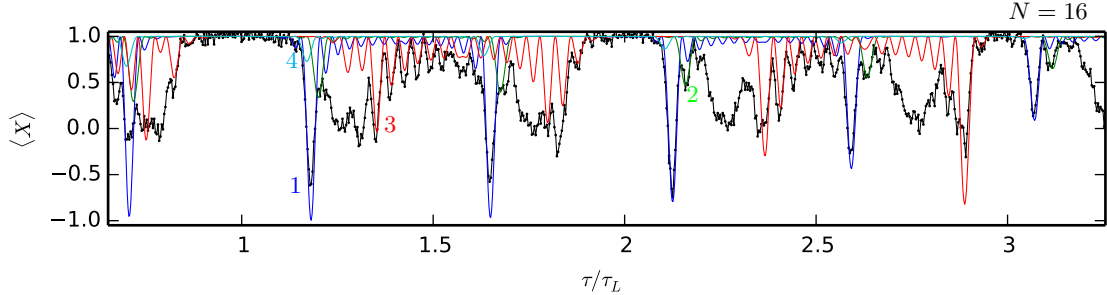
At the edges of this collapse several sharp dips are visible. These correspond to individual spins.

¹ $F|0\rangle > 0.68$

Between the broad collapses there alternately appears an oscillation. This oscillation is caused by a spin in the complex regime.

The physical processes resulting in such a fingerprint will be discussed in the next section.

(a)



(b)

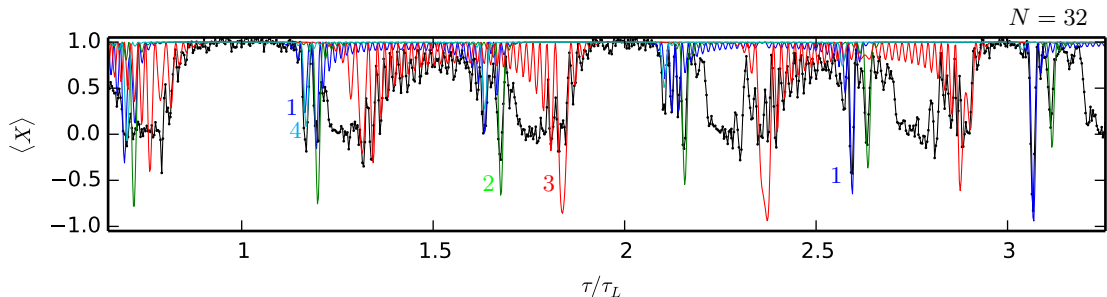


Figure 3.2 – Part of a dynamical decoupling spectroscopy experiment performed at $B_z = 304$ G, $\tau_L = 3.07\ \mu\text{s}$. Black lines correspond to data. Colored lines represent computed responses of carbon spins. (a) $N = 16$ pulses; (b) $N = 32$ pulses. Contrast is lowered when the decoupling sequence performs an entangling operation on a spin in the environment. A reference to the full dynamical decoupling dataset can be found in Appendix A.2. Responses were calculated using Eq. (A.2) with hyperfine parameters from Table 3.1.

3.2.2 The effect of dynamical decoupling on nuclear spins

During dynamical decoupling the electronic state alternates between the $m_s = 0$ and $m_s = +1$ state, this causes the nuclear spin to alternately rotate around two distinct quantization axes (Fig. 3.3). When the electron is in the $m_s = 0$ state each nuclear spin precesses about ω_L with the Larmor frequency given by Eq. (2.5). When the electron is in the $m_s = +1$ state there is a hyperfine interaction between the nucleus and the NV-center (Eq. (2.4)) and the spin precesses around $\tilde{\omega} = \omega_L + \mathbf{A}$, where $\mathbf{A} = A_{||}\hat{\mathbf{z}} + A_{\perp}\hat{\mathbf{x}}$ [25].

The result of a decoupling sequence is a net rotation around an axis $\hat{\mathbf{n}}_i$ by an angle θ . Where $\hat{\mathbf{n}}_i$ depends on the initial state of the electron and θ is proportional to the number of pulses N [25]. $\hat{\mathbf{n}}_i = \hat{\mathbf{n}}_0$ when the electron starts in $m_s = 0$ and $\hat{\mathbf{n}}_i = \hat{\mathbf{n}}_1$ when the electron starts in $m_s = +1$.

When the net rotation axes point in a different direction a conditional operation is executed during dynamical decoupling (Fig. 3.4). In a dynamical decoupling spectroscopy contrast is lowered when a conditional operation is executed. To understand when this occurs it is useful to consider two different regimes for carbon spins: the basic regime where $A_{\perp} \ll \omega_L$ and the complex regime where $A_{\perp} \sim \omega_L$. For a mathematical description of the result of a dynamical decoupling spectroscopy the reader is referred to Appendix A.1.

The basic regime ($A_{\perp} \ll \omega_L$)

In the basic regime the net rotation axes are practically parallel and point in the z -direction for almost every τ except for a specific resonant condition for which the axes are anti-parallel. This

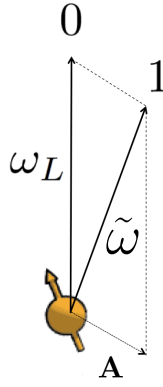


Figure 3.3 – Flipping the electron spin from the $m_s = 0$ to the $m_s = +1$ state changes the quantization axis of nuclear spins. For $m_s = 0$ all nuclear spins precess about ω_L . For $m_s = +1$ each spin precesses about a distinct axis $\tilde{\omega} = \omega_L + \mathbf{A}$ due to the hyperfine interaction.

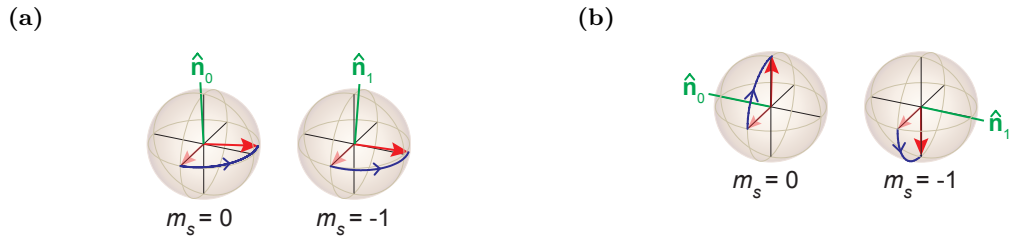


Figure 3.4 – (a) When the net rotation axes \hat{n}_0 and \hat{n}_1 point in the same direction the carbon experiences an unconditional rotation. (b) When the net rotation axes \hat{n}_0 and \hat{n}_1 are anti-parallel the carbon experiences a conditional rotation, either around $+x$ or $-x$. Figure from Taminiau et al. [25].

resonant condition is given by Eq. (3.1):

$$\tau = \frac{(2k+1)\pi}{2\omega_L + A_{||}} \quad (3.1)$$

Where k is an integer, and has a Lorentzian shape in a dynamical decoupling spectroscopy. These sharp resonances are the origin of the sharp dips in the dynamical decoupling spectroscopy. The FWHM of the resonance is given by Eq. (3.2):

$$\text{FWHM}_{\text{DD}} = \frac{A_{\perp}}{2\omega_L^2} \quad (3.2)$$

The complex regime ($A_{\perp} \sim \omega_L$)

In the case where ω_L and A_{\perp} are of comparable magnitude the net rotation axes are strongly dependent on the initial electron-state for almost any τ . When a carbon is in this regime it is no longer possible to describe it as a narrow resonance in the dynamical decoupling spectroscopy. The response is visible as a wide resonance with an oscillation on top of it, spin 3 in Fig. 3.2 is an example of such a spin.

When the response of multiple carbon spins in a dynamical decoupling spectroscopy overlaps, the electron performs an entangling operation on all these carbons. Because of this the measured contrast in a dynamical decoupling spectroscopy goes down rapidly when the responses of multiple carbons overlap. This makes it hard to resolve individual spins when a spin has a broad response, such as a spin in the complex regime, or if there are several spins with similar hyperfine couplings.

3.2.3 Identifying Individual Carbon-spins

Using the previous section it is possible to identify individual spins. A first estimate of the hyperfine coupling to these spins can be made based on the location and width of dips in the dynamical decoupling spectroscopy using Eqs. (3.1) and (3.2). By computing the responses for the hyperfine

parameters using Eq. (A.2) the estimation can be improved. Using this method 13 distinct carbon spins were identified.

The parameters of the 4 strongest coupled carbons are listed in Table 3.1 and their computed responses are visible as colored lines in Fig. 3.2. All estimated hyperfine parameters and a link to the full dynamical decoupling dataset can be found in Appendix A.2.

Table 3.1 – Estimated hyperfine parameters for spins 1 to 4 in Fig. 3.2.

Carbon	A_{\parallel}	A_{\perp}
1	$2\pi \cdot 30.0$ kHz	$2\pi \cdot 80.0$ kHz
2	$2\pi \cdot 27.0$ kHz	$2\pi \cdot 28.5$ kHz
3	$2\pi \cdot 51.0$ kHz	$2\pi \cdot 105.0$ kHz
4	$2\pi \cdot 45.1$ kHz	$2\pi \cdot 20.0$ kHz

3.3 Characterizing weakly-coupled carbon spins

Using the knowledge of the interaction between the NV-center and individual nuclear spins it is possible to implement basic gates and characterize the spins. This section will first explain how basic gates can be implemented on weakly coupled carbon spins. These gates are then used to measure the precession frequencies and T_2^* for individual carbon spins.

In order to implement gates with the correct phase we calculate the state evolution. For this we need to know the precession frequency during dynamical decoupling (ω_{DD}) as well as the precession frequency when the electron is in $|0\rangle$ (ω_L) or $|1\rangle$ ($\tilde{\omega}$). ω_{DD} is used to calculate the phase when operations are applied to the nuclear spins. The precession frequencies corresponding to the eigenstates are used to calculate phase evolution during readouts.

3.3.1 Basic operations

In order to implement basic gates on a nuclear spin we make use of the conditional rotation that occurs on the resonance given by Eq. (3.1). At the resonant condition the nuclear spin rotates about one of two anti-parallel axes depending on the electronic-spin state. The angle of the rotation is proportional to the number of pulses on the electron (N). By sweeping the number of pulses to perform a $\pi/2$ rotation a maximally entangling gate is performed. We define the axis of rotation of this operation as the x -axis and call the operation the $\pm x$ -gate.

By bringing the electron in a superposition, sweeping the number of pulses on the electron and measuring the contrast an oscillation can be measured as the electron spin repeatedly entangles and disentangles with the carbon spin. This oscillation can be used to calibrate the $\pm x$ -gate.

The $\pm x$ -gate forms the basis of our control over weakly coupled spins. Figure 3.5 shows how the $\pm x$ -gate is depicted in a circuit-diagram. By letting the phase of the carbon evolve we are able to apply operations on the carbon-spin with arbitrary phase.

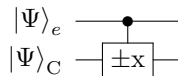


Figure 3.5 – The $\pm x$ -gate performs an x -rotation on the carbon ($|\Psi\rangle_C$) when the electron is in the $|0\rangle_e$ -state. It performs a $-x$ -rotation when the electron is in the $|1\rangle_e$ -state.

The $\pm x$ -gate has been calibrated for several spins. The parameters used to implement $\pm x$ -gates are listed in Table 3.2. Of these carbon-1 and carbon-4 were selected for the experiments.

Table 3.2 – Parameters used to implement $\pm x$ -gates.

Carbon	N	τ	total gate time
1	18	$9.420 \mu s$	$339 \mu s$
2	26	$6.620 \mu s$	$344 \mu s$
3	14	$18.564 \mu s$	$520 \mu s$
4	40	$6.456 \mu s$	$516 \mu s$

3.3.2 Carbon Ramsey experiment

By performing a Ramsey experiment the precession frequencies and the dephasing-time T_2^* can be determined. The precession frequencies are required to calculate the phase required to implement operations with the correct phase. By measuring the precession frequency it is also possible to test our estimation for the hyperfine parameters.

In an ordinary Ramsey experiment a qubit is brought to the equator of the Bloch-sphere where it precesses for a time τ before it is read out along the x-direction. We perform a similar experiment without initializing the carbon spin.

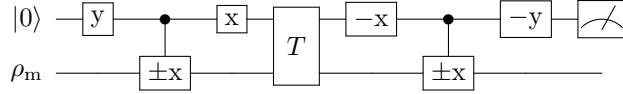


Figure 3.6 – Gate circuit depicting an uninitialized carbon Ramsey. T is the free evolution time. x and y are $\pi/2$ pulses along the x and y axis respectively.

The gate circuit of the uninitialized carbon-Ramsey experiment is depicted in Fig. 3.6. The first pulse brings the electronic spin in the $|X\rangle$ -state. Because the carbon starts out in a mixed state the two-qubit system can be described by the tensor product of two density matrices:

$$\rho_X \otimes \rho_m = \rho_X \otimes \rho_X + \rho_X \otimes \rho_{-X} \quad (3.3)$$

By applying the $\pm x$ -gate the electronic-spin picks up a phase depending on the nuclear spin-state:

$$\rho_Y \otimes \rho_X + \rho_{-Y} \otimes \rho_{-X} \quad (3.4)$$

In this state it is either left to freely evolve for a time T before a $\pi/2$ -pulse is applied to bring the electron back to the poles of the Bloch-sphere. If the extra $\pi/2$ -pulse is applied the system is in the following state before the free evolution.

$$\rho_0 \otimes \rho_X + \rho_1 \otimes \rho_{-X} \quad (3.5)$$

Because the electronic spin is in a different state for ρ_X and ρ_{-X} they evolve with different frequencies. After the free evolution another $\pi/2$ -pulse is applied to bring the electronic spin back into the xy -plane.

The final part of the circuit reads out the nuclear spin along the x-direction. The phase picked up during free evolution shows up as an oscillation between $|0\rangle_e$ and $|1\rangle_e$ in the readout.

Determining the precession frequency

Because the uninitialized carbon-Ramsey evolves with two frequencies we expect the measured oscillation to be the sum of two cosines as described by Eq. (3.6):

$$c_1 - c_2 \cos(\omega_L \tau) - c_3 \cos(\tilde{\omega} \tau) \quad (3.6)$$

Where $\tilde{\omega} = \sqrt{(\omega_L + A_{\parallel})^2 + A_{\perp}^2}$ and c_1 , c_2 and c_3 are constants.

Figure 3.7 shows the results for a carbon-Ramsey experiment without initialization of the nucleus. The data was fitted to a sum of two cosines in order to determine the frequencies.

The Larmor frequencies measured are $\omega_{L,C1} = 2\pi \cdot 325.81 \pm 0.25$ kHz for carbon-1 and $\omega_{L,C4} = 2\pi \cdot 325.94 \pm 0.40$ kHz for carbon-4. Both the measured Larmor frequencies agree with the magnetic field of 304 G within two standard deviations.

Based on the estimated hyperfine parameters we expect $\tilde{\omega}_{C1} \approx 2\pi \cdot 364.7$ kHz for carbon-1 and $\tilde{\omega}_{C4} \approx 2\pi \cdot 371.4$ kHz for carbon-4. For carbon-1 $\tilde{\omega}_{C1} = 2\pi \cdot 364.41 \pm 0.23$ kHz was measured and for carbon-4 $\tilde{\omega}_{C4} = 2\pi \cdot 371.52 \pm 0.39$ kHz was measured. Both these values are in good agreement with experiment, an indication that our hyperfine estimation is accurate.

Measuring $T_{2,C}^*$

To determine $T_{2,C}^*$ for normal operation an uninitialized carbon-Ramsey was performed where the electron was dynamically decoupled during the free evolution time. The uninitialized carbon-Ramsey with decoupling differs from the uninitialized carbon-Ramsey without decoupling in that two $\pi/2$ pulses are missing and the electron is decoupled during the free evolution time. A gate

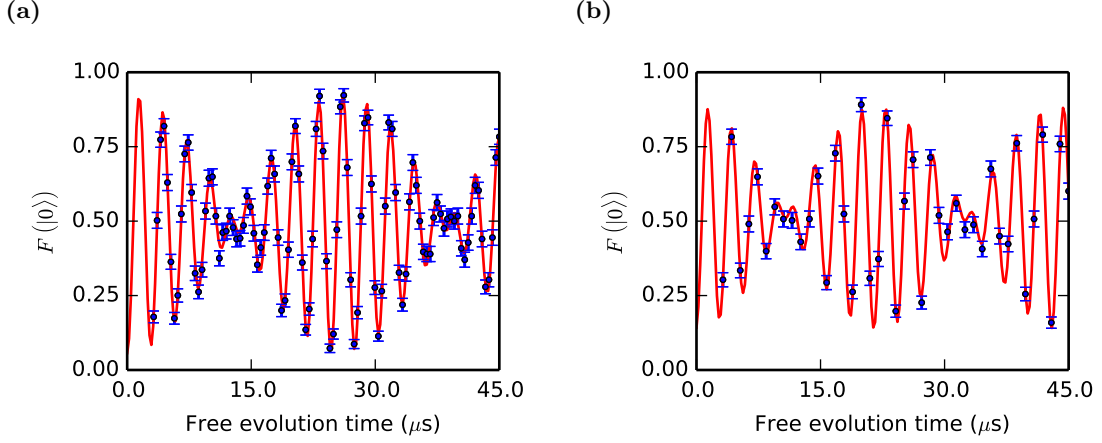


Figure 3.7 – The uninitialized carbon-Ramsey experiment shows an oscillation due to the phase picked up during free evolution. (a) shows data for carbon-1 and (b) for carbon-4.

circuit describing the experiment is visible in Fig. 3.8. Dynamical decoupling was performed at $\tau = 8 \cdot \tau_L$ by varying the number of pulses N . τ_L is the Larmor period $1/\omega_L$ of the carbon. Because the electron is constantly flipped the carbon will precess with an average frequency of $\omega_{DD} \approx (\omega_L + \tilde{\omega})/2$. By undersampling with a frequency slightly detuned from the precession frequency (ω_{DD}) a decaying cosine can be observed where the $1/e$ time of the envelope is equal to T_2^* . Because this decaying cosine can be measured for a relatively long time (\sim ms) this method can also be used to accurately determine the precession frequency ω_{DD} .

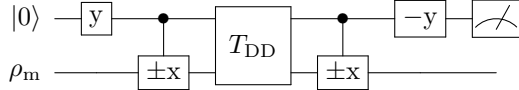


Figure 3.8 – Gate circuit depicting an uninitialized carbon Ramsey with decoupling. T_{DD} is the free evolution time. x and y are $\pi/2$ pulses along the x and y axis respectively.

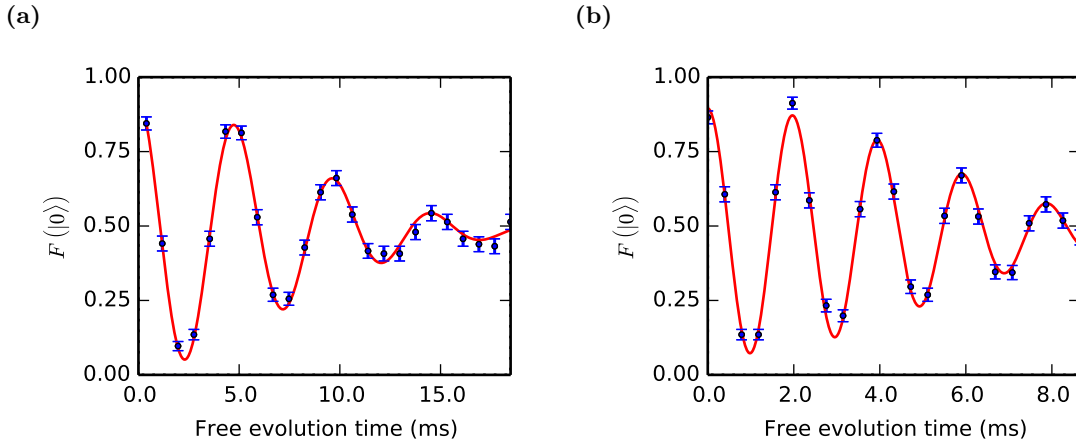


Figure 3.9 – Carbon-Ramsey experiment to determine T_2^* for nuclei while decoupling the electron. Dynamical decoupling during evolution is implemented at $8 \cdot \tau_L$ of the carbon spin. The free evolution time is varied by varying the number of pulses. The decays are fitted with a generalized normal distribution to determine T_2^* and the exponent n . (a) Ramsey decay for carbon-1, $T_{2,C1}^* = 9.85 \pm 0.39$ ms and $n = 1.83 \pm 0.19$. (b) Ramsey decay for carbon-4, $T_{2,C4}^* = 6.68 \pm 0.22$ ms and $n = 2.31 \pm 0.31$.

Figure 3.9 shows the decay for both carbons. The decay follows a Gaussian profile within uncertainty for both spins. The coherence times measured were $T_{2,C1}^* = 9.85 \pm 0.39$ ms for carbon-1 and $T_{2,C4}^* = 6.68 \pm 0.22$ ms for carbon-4. It should be noted that these T_2^* values are not limited by the electron coherence which was measured to be larger than 40 ms for $N = 256$ pulses.

4

Entangling Weakly-coupled Carbon Spins

The capability to perform parity measurements is essential for QEC in particular and quantum-computation in general. This chapter demonstrates how weakly coupled carbon spins can be initialized and read-out and creates entanglement between two weakly coupled spins through a parity measurement. The creation of entanglement serves to demonstrate that the parity measurement was successfully implemented.

4.1 Initialization and readout of single spins

We initialize spins by measurements. A weakly coupled carbon spin can be measured by entangling the phase of the electronic-spin with the state of the carbon spin and reading out the phase of the electronic spin.

The gates used to initialize a weakly coupled carbon are depicted in Fig. 4.1. The circuit depicted in Fig. 4.1a projects the carbon spin along the x -axis upon readout of the electronic spin. By adding an additional conditional gate, as depicted in Fig. 4.1b, the carbon spin is brought into the $|0\rangle$ -state regardless of the measurement outcome of the electronic spin. In that case the electron measurement is used to reinitialize the electron.



Figure 4.1 – (a) MBI-based initialization into $\pm|X\rangle$. Initializes the carbon into $|X\rangle_C$ when $|0\rangle_e$ is measured and into $|-X\rangle_C$ when $|1\rangle_e$ is measured for the electron. (b) MBI-swap initialization into $|0\rangle$. Initializes the carbon into $|0\rangle_C$ regardless of the electronic spin-state measured.

To initialize the carbon spin an initial pulse brings the electronic spin in $|X\rangle_e$. When the carbon spin starts in the mixed state the system can be described by the tensor product of two density matrices:

$$\rho_X \otimes \rho_m = \rho_X \otimes \rho_X + \rho_X \otimes \rho_{-X} \quad (4.1)$$

By applying the $\pm x$ -gate the electronic-spin picks up a phase depending on the carbon spin-state:

$$\rho_Y \otimes \rho_X + \rho_{-Y} \otimes \rho_{-X} \quad (4.2)$$

By reading out the electronic spin along the y -axis the carbon spin is projected into the $|X\rangle_C$ or $|-X\rangle_C$ -state. This correlates the electronic-spin readout to the x -projection of the carbon spin. By conditioning on a positive readout result the state can be initialized into the $|X\rangle_C$ -state. By applying an additional $\mp y$ gate the carbon spin can be initialized into $|0\rangle$.

A weakly coupled carbon spin can be read out along the x -direction using the same circuit as used to initialize into $|X\rangle$. By changing the conditional gate to $\pm y$ the carbon can be read out along y . In order to read out the carbon along the z -direction an additional $\pm z$ -gate is added before the initial y -pulse (Fig. 4.2). It should be noted that the z -readout does not leave the carbon spin in $|0\rangle$ or $|1\rangle$ but in $|X\rangle$ or $|-X\rangle$.

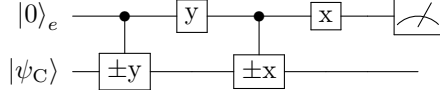


Figure 4.2 – Gate circuit used to read out a carbon spin along z . The initial $\pm y$ rotates the state onto the x -basis. The rest of the circuit is identical to the circuit in Fig. 4.1a and is used to read out the carbon spin along x .

Figure 4.3 demonstrates experimental initialization and readout of a carbon spin. In Fig. 4.3a carbon-1 is initialized into the $|X\rangle_C$ -state and in Fig. 4.3b it is initialized into the $|0\rangle_C$ -state. This is done by implementing the circuits depicted in Fig. 4.1 and conditioning on a positive electron readout result.

The blue points correspond to x -readout, the green points to y -readout and the red-points to the z -readout. The phase is swept to demonstrate that the readouts function as intended. For a qubit in the $|0\rangle$ -state the initial phase is undefined.

The combined fidelity of readout and initialization to the desired state is: $F(|X\rangle) = 90.57 \pm 0.85\%$ for the $|X\rangle$ -state and $F(|Z\rangle) = 93.00 \pm 0.31\%$ for the $|Z\rangle$ -state.

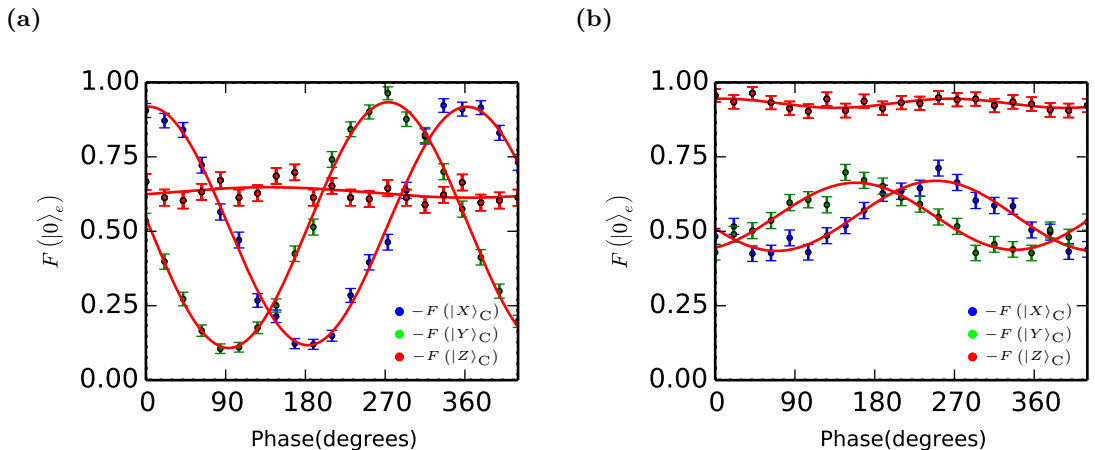


Figure 4.3 – Demonstration of carbon initialization and readout. In (a) carbon-1 is initialized in $|X\rangle$. In (b) carbon-1 is initialized in $|0\rangle$. Colored points correspond to readouts in different bases, blue to x -readout, green to y -readout and red to z -readout. The red lines are fits to the data with a cosine: $a + A \cos(\phi + \phi_0)$.

4.2 Parity measurements

Entanglement between two qubits can be created by performing a parity measurement on them and conditioning on the outcome.

A parity measurement measures if two qubits are correlated in a certain basis. An example is the XX-parity measurement. The XX-parity measurement returns a positive result if the two qubits are parallel along x and a negative result if the two are anti-parallel. That is it returns a positive result if the state is a linear combination of $|X, X\rangle$ and $|-, -\rangle$ and a negative result if the state is a linear combination $|X, -\rangle$ and $|-, X\rangle$. In general a two qubit parity operator has 2 eigenvalues, both are twofold degenerate.

The XX-parity measurement can be implemented on a weakly coupled carbon spins using the circuit depicted in Fig. 4.4. A parity measurement is similar to the regular readout depicted in Fig. 4.1a. Once the electron is brought into a superposition the electron picks up a phase when the $\pm x$ -gate is applied: $+\pi/2$ -phase when the carbon is in $|+X\rangle$ and $-\pi/2$ -phase when the carbon is in $|-, -\rangle$. This is done for both carbons, when both carbons are in the same x -state the electron will pick up π -phase. When they do not give the same result the phase cancels. By reading out the electronic-spin along x the parity is measured. It should be noted that because we use a $\pm x$ -gate instead of a CNOT-gate an additional $\pi/2$ -phase is added to the carbon states. For the odd parity measurements considered in the experiments this is of no concern as the phase cancels out.

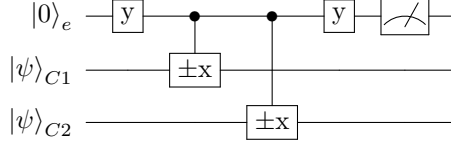


Figure 4.4 – Gate circuit for a XX-parity measurement.

4.3 Quantum state tomography

In this thesis the entangled state is verified by performing a quantum state tomography. In a quantum state tomography the density matrix of a quantum state is reconstructed by repeatedly preparing the same state and gathering measurement statistics in different bases.

An arbitrary density matrix can be described as a weighted sum of the Pauli-matrices and the Identity Eq. (4.3):

$$\rho = \frac{1}{4} \sum_{i,j} a_{i,j} \sigma_i \otimes \sigma_j, \quad \text{for } \sigma_i, \sigma_j \in \{I, X, Y, Z\} \quad (4.3)$$

By measuring the coefficients $a_{i,j} = \langle \sigma_i, \sigma_j \rangle$ the density matrix ρ can be reconstructed completely.

4.3.1 Readout

To measure the required experimental values single and multi qubit measurements are needed. Single qubit measurements were described in Section 4.1. The two qubit measurements required are very similar to parity measurements but do not necessarily need to preserve the state after the measurement.

The parity measurement depicted in Fig. 4.4 is used to measure the XX-parity. By changing the phase of one of the two $\pm x$ gates a Y-parity can be measured. By applying a $\mp y$ to one of the two carbons before the initial y -pulse a Z-parity can be measured. As an example Fig. 4.5 implements the YZ-parity measurement.

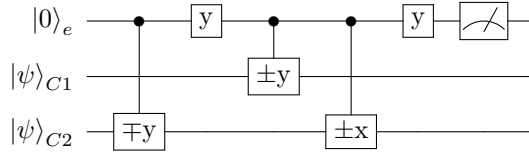


Figure 4.5 – Example of a parity measurement that measures the YZ-parity.

4.3.2 Initialization and tomography of multiple weakly coupled spins

The tomography is performed on two initialized two-qubit states. The combined fidelity of the initialization and tomography is calculated by comparing to the ideal case.

Figure 4.6a shows a tomography of carbon-1 and carbon-4 initialized in the $|00\rangle$ -state. In the ideal case the single qubit Z-measurements and the ZZ parity are 1 and all other coefficients are 0. The ideal case is represented by the gray bars in the Fig. 4.6a. The fidelity to the ideal case is $F = 81.43 \pm 1.68 \%$.

Figure 4.6b shows a tomography of carbon-1 and carbon-4 initialized in the $|01\rangle$ -state. In the ideal case ZI = 1 and IZ and ZZ are -1, all other coefficients are 0. The ideal case is represented by the gray bars in the Fig. 4.6b. The fidelity to the ideal case prediction is $80.99 \pm 1.69 \%$.

4.4 Demonstrating entanglement between weakly coupled carbons

We combine multi-qubit initialization, parity measurements and the quantum state tomography to demonstrate entanglement. After the qubits are initialized an XX-parity is performed and the tomography is conditioned on the negative electron readout result. The experiment is done for carbons initialized in $|00\rangle$ and carbons initialized in $|01\rangle$.

By conditioning on the negative readout result the carbons are projected into the negative-parity eigenspace of the XX-parity operator: $|-X, X\rangle$ and $|+X, X\rangle$. Ideally the tomography correlation

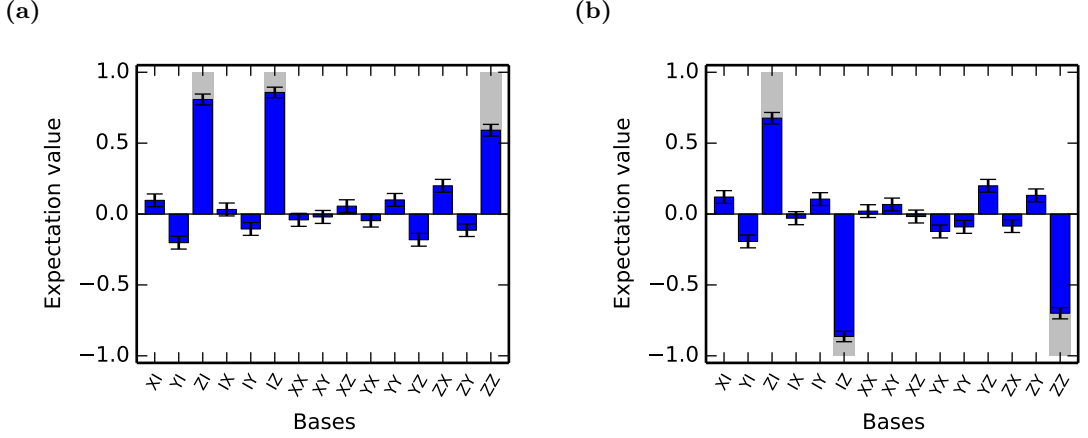


Figure 4.6 – Quantum state tomographies of two initialized carbons. In (a) the carbons are initialized into $|00\rangle$ with a fidelity of $81.43 \pm 1.68\%$. In (b) the carbons are initialized into $|10\rangle$ with a fidelity of $80.99 \pm 1.69\%$.

for the XX-parity is -1. The other coefficients depend on the initial state the parity was performed on.

Figure 4.7a shows the tomography for the negative XX parity of the $|00\rangle$ -state. $|00\rangle$ can be written in the x -basis as:

$$|00\rangle = \frac{1}{2} (|X, X\rangle + |X, -X\rangle + |-X, X\rangle + |-X, -X\rangle) \quad (4.4)$$

By measuring the negative XX-parity the state is projected onto:

$$\Psi = \frac{1}{\sqrt{2}} (|X, -X\rangle + |-X, X\rangle) \quad (4.5)$$

In the y -basis this state can be written as:

$$\Psi = \frac{1}{\sqrt{2}} (|Y, Y\rangle + |-Y, -Y\rangle) \quad (4.6)$$

And in the z -basis this is:

$$\Psi = \frac{1}{\sqrt{2}} (|00\rangle - |11\rangle) \quad (4.7)$$

It follows that $\langle YY \rangle = \langle ZZ \rangle = +1$. The fidelity to the ideal case prediction is $76.60 \pm 1.74\%$.

Figure 4.7b shows the tomography for the negative XX parity of the $|01\rangle$ -state. $|01\rangle$ can be written in the X -basis as:

$$|01\rangle = \frac{1}{2} (|X, X\rangle - |X, -X\rangle + |-X, X\rangle - |-X, -X\rangle) \quad (4.8)$$

By measuring the negative XX-parity the state is projected onto:

$$\Phi = \frac{1}{\sqrt{2}} (|-X, X\rangle - |X, -X\rangle) \quad (4.9)$$

In the yy -basis this state can be written as:

$$\Phi = \frac{i}{\sqrt{2}} (|Y, -Y\rangle - |-Y, Y\rangle) \quad (4.10)$$

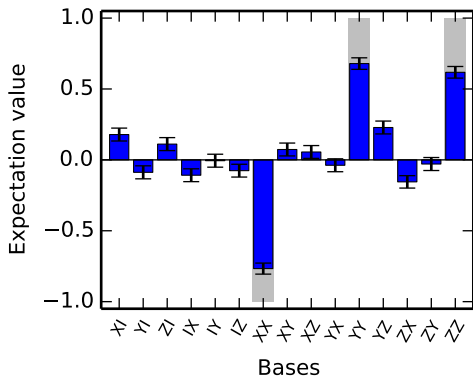
And in the zz -basis this is:

$$\Phi = \frac{1}{\sqrt{2}} (|10\rangle - |01\rangle) \quad (4.11)$$

It follows that $\langle YY \rangle = \langle ZZ \rangle = -1$. The fidelity to the ideal case prediction is $76.08 \pm 1.74\%$.

Both measured parities show a fidelity to respective Bell-state well above 0.5, demonstrating that the states are entangled and that the parity measurement is successfully implemented.

(a)



(b)

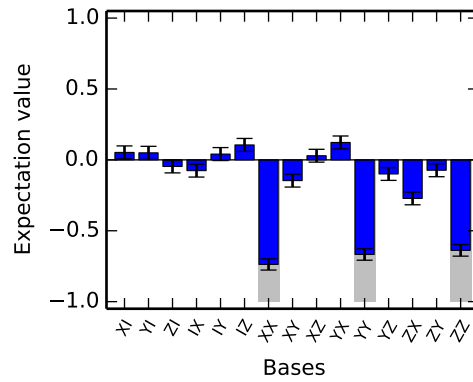


Figure 4.7 – Quantum state tomographies for entangled states created by measuring a negative XX parity. (a) is the negative XX-parity of the state prepared in (a). It is projected into $\frac{1}{\sqrt{2}}(|X, -X\rangle + |X, -X\rangle)$ with $76.60 \pm 1.74\%$ fidelity. (b) is the negative XX-parity of the state prepared in (b). It is projected into $\frac{1}{\sqrt{2}}(|X, -X\rangle - |X, -X\rangle)$ with $76.08 \pm 1.74\%$ fidelity.

5

Towards Quantum Error Correction

In this thesis we demonstrated the implementation of a parity measurement between two weakly coupled carbons spin. Two more challenges remain to realize quantum error correction. First, to correct errors, gate operations that are conditional on the parity outcome are required. Therefore the parity measurement must be accurate and preserve entangled state for both outcomes [?], unlike the probabilistic initialization and entanglement in this thesis.

Second, for error correction encoding in larger entangled states is required: at least three qubits for the simplest error correction and at least five qubits for correction of all types of errors. In this chapter I address these two challenges and present simulations that indicate that multi-qubit parity measurements on weakly coupled spins are possible.

5.1 Deterministic Parity Measurements

An essential capability for QEC is the ability to perform different quantum operations based on a classical readout result. An example of such an experiment is the deterministic creation of entanglement, as was demonstrated by [?] in a different system.

By applying an extra set of gates when the negative result is measured in a parity measurement the state can be transformed in the state that would have been created had the positive parity been measured. This capability is particular important for QEC where the result of a parity measurement determines whether a correcting gate must be applied.

The main challenge when performing such operations is to keep track of the phase of the system during the readout that determines which set of gates should be executed. The measurement environment developed for the work in this thesis automatically keep track of phases and has been set up to be extendable and compatible with such feed forward capabilities.

5.2 Multi Qubit Control

In order to implement QEC more than the two qubits that were addressed are required. To correct for a single type of quantum error 3 qubits are required. To correct for any type of quantum error at least 5 qubits are required.

5.2.1 Overview of the simulations

Simulations were performed to determine how many weakly coupled carbons can be controlled, on average, for an NV-center using dynamical decoupling. In the simulations statistics were collected on 1000 NV-centers for a range of magnetic fields and three different carbon-13 concentrations. For all NV-centers an environment of carbon-13 spins randomly placed on lattice points was generated. For lower concentrations a larger environment was simulated such that the total number of simulated carbon spins was ~ 300 per NV-center for all concentrations.

NV-centers containing a carbon with a hyperfine coupling larger than 200 kHz were rejected as such spins are prone to decohere during the optical readout of the electron spin [18] and their complex dynamics at moderate field complicate spin control of other spins (Chapter 3). In an experimental setting these carbons can be easily detected and the NV-centers rejected.

On the remaining centers the hyperfine coupling between each carbon and the NV-center as well as the resonance conditions of these carbons were calculated. At these resonances it was determined if a carbon can be selectively and coherently controlled.

As a figure of merit we take the fidelity F of the electron spin after two consecutive $\pm x$ gates. The first gate entangles the electron spin with the nuclear spin and the second gate disentangles the two. Reduced electron spin fidelity indicates gate imperfections or unwanted entanglement of the electron to the other carbon-13 spins. The threshold for a carbon-13 to be considered controllable is set at $F = 90\%$.

The fidelity is determined by sweeping the number of pulses at the resonance conditions and determining with what fidelity two consecutive $\pm x$ -gates can be implemented. The accuracy with which the resonance can be addressed is limited by the resolution of the arbitrary waveform generator at 1 ns. The fidelity is determined under the assumption of perfect π and $\pi/2$ pulses on the electron.

Additionally we require to be able to perform 10 such gates within the coherence time. For simplicity we do not simulate the nuclear-nuclear interactions and instead set T_2^* as in Table 5.1. Finally, we set a maximum value for the inter pulse delay τ_{\max} , to take into account the limited coherence for the electron at large τ . τ_{\max} is set at the values listed in Table 5.1.

Table 5.1 – Coherence times and maximum resonance time as used in the simulations.

Concentration	$T_{2,C}^*$	τ_{\max}
1.10 %	7ms	10 μ s
0.33 %	45ms	36.7 μ s
0.11 %	70ms	100 μ s

5.2.2 Results of the simulation

Figure 5.1a shows the average number of addressable carbon spins as a function of magnetic field. The number of addressable carbons increases quickly at first before a slow decay sets in.

The initial increase in the number of addressable carbons can be explained by the Larmor frequency becoming larger than the hyperfine interaction. At low magnetic field ($\omega_L \sim A$) most spins undergo complex dynamics. When the Larmor frequency becomes larger than the hyperfine coupling of a carbon spin it is in the simple regime where the resonances are narrow. Because there is less overlap more spins can be addressed. This increase drops off because eventually all spins are in the simple regime.

By increasing the magnetic field further the resonances both get narrower (Eq. (3.2)) and move to shorter times (Eq. (3.1)). When the field becomes too high a resonance can become too narrow to accurately address. This is limited by the 1 ns timing resolution of the arbitrary waveform generator. Therefore the number of addressable spins decreases at high fields.

For lower concentrations there are on average less spins undergoing complex dynamics for the same magnetic field. This causes the initial increase in addressable carbons to be steeper at lower concentrations.

There is also a bias due to the rejection of carbons with $|A| > 200$ kHz. Not rejecting these carbons will lower the number of addressable carbons for low magnetic fields as the response of these carbons dominates the dynamical decoupling spectroscopy, while the number of addressable carbons will increase slightly in the high field limit were these carbons can be controlled through dynamical decoupling.

Figure 5.1b shows the distribution of addressable carbons for a natural concentration of carbon-13 at the magnetic field that has the highest average number of addressable carbons. It indicates that in most NV-centers (89 %) three or more carbons can be addressed and that in a reasonable fraction (57 %) of the samples five or more carbons can be addressed. There are even rare occurrences where ten or more carbons can be addressed.

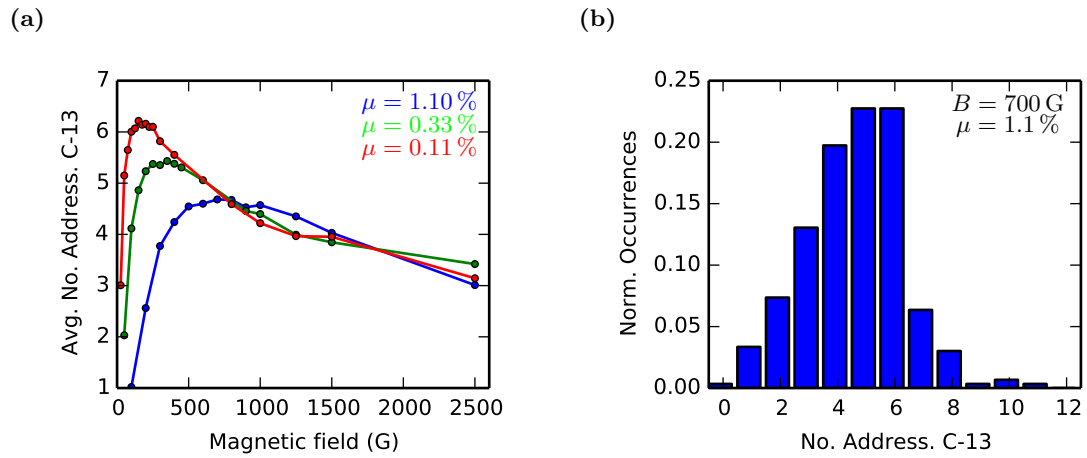


Figure 5.1 – Simulation results calculating the number of addressable carbons in NV-centers containing no carbons with hyperfine coupling larger than 200 kHz. (a) Average number of addressable carbons at different concentrations. (b) Normalized occurrences for $\mu = 1.1\%$ at 700 G. The simulation indicates that an NV-center likely has 3 or more addressable carbons($P = 89\%$), that there is a good chance that 5 or more carbons can be addressed ($P = 57\%$) and that there is even a small probability of getting ~ 10 addressable carbon spins.

Bibliography

- [1] N. Bar-Gill, L. M. Pham, A. Jarmola, D. Budker, and R.L. Walsworth. Solid-state electronic spin coherence time approaching one second. *Nature communications*, 4:1743, 1 2013. ISSN 2041-1723. URL <http://www.ncbi.nlm.nih.gov/pubmed/23612284>.
- [2] H. Bernien. *Control, Measurement and Entanglement of Remote Quantum Spin Registers in Diamond*. PhD thesis, Delft University of Technology, 2014.
- [3] H. Bernien, B. Hensen, W. Pfaff, G. Koolstra, M. S. Blok, L. Robledo, T. H. Taminiau, M. Markham, D. J. Twitchen, L. Childress, and R. Hanson. Heralded entanglement between solid-state qubits separated by three metres. *Nature*, 497(7447):86–90, 5 2013. ISSN 1476-4687. URL <http://www.ncbi.nlm.nih.gov/pubmed/23615617>.
- [4] L. Childress and R. Hanson. Diamond nv centers for quantum computing and quantum networks. *MRS Bulletin*, 38(02):134–138, 2 2013. ISSN 0883-7694. URL http://www.journals.cambridge.org/abstract_S0883769413000201.
- [5] D. Cory, M. Price, W. Maas, E. Knill, R. Laflamme, W. Zurek, T. Havel, and S. Somaroo. Experimental quantum error correction. *Physical Review Letters*, 81(10):2152–2155, 9 1998. ISSN 0031-9007. URL <http://link.aps.org/doi/10.1103/PhysRevLett.81.2152>.
- [6] G. de Lange. *Quantum Control and Coherence of Interacting Spins in Diamond*. PhD thesis, Delft University of Technology, 2012.
- [7] G. de Lange, Z.H. Wang, D. Ristè, V.V. Dobrovitski, and R. Hanson. Universal dynamical decoupling of a single solid-state spin from a spin bath. *Science (New York, N.Y.)*, 330(6000):60–3, 10 2010. ISSN 1095-9203. URL <http://www.ncbi.nlm.nih.gov/pubmed/20829452>.
- [8] R.P. Feynman. Simulating physics with computers. *International Journal of Theoretical Physics*, 21(6-7):467–488, 6 1982. ISSN 0020-7748. URL <http://link.springer.com/10.1007/BF02650179>.
- [9] A.G. Fowler, M. Mariantoni, J.M. Martinis, and A.N. Cleland. Surface codes: Towards practical large-scale quantum computation. *Physical Review A*, 86(3):032324, 9 2012. ISSN 1050-2947. URL <http://link.aps.org/doi/10.1103/PhysRevA.86.032324>.
- [10] A. Gali. Identification of individual isotopes of nitrogen-vacancy center in diamond by combining the polarization studies of nuclear spins and first-principles calculations. *Physical Review B*, 80(24):241204, 12 2009. ISSN 1098-0121. URL <http://link.aps.org/doi/10.1103/PhysRevB.80.241204>.
- [11] A. Gali, M. Fyta, and E. Kaxiras. Ab initio supercell calculations on nitrogen-vacancy center in diamond: Electronic structure and hyperfine tensors. *Physical Review B*, 77(15):155206, 4 2008. ISSN 1098-0121. URL <http://link.aps.org/doi/10.1103/PhysRevB.77.155206>.
- [12] B.J. Hensen. Measurement-based quantum computation with the nitrogen-vacancy centre in diamond. Master’s thesis, Delft University of Technology, 2011.

- [13] F. Jelezko, T. Gaebel, I. Popa, A. Gruber, and J. Wrachtrup. Observation of coherent oscillations in a single electron spin. *Physical Review Letters*, 92(7):076401, 2 2004. ISSN 0031-9007. URL <http://link.aps.org/doi/10.1103/PhysRevLett.92.076401>.
- [14] N.D. Mermin. Extreme quantum entanglement in a superposition of macroscopically distinct states. *Physical Review Letters*, 65(15):1838–1840, 10 1990. ISSN 0031-9007. URL <http://link.aps.org/doi/10.1103/PhysRevLett.65.1838>.
- [15] O. Moussa, J. Baugh, C. A. Ryan, and R. Laflamme. Demonstration of sufficient control for two rounds of quantum error correction in a solid state ensemble quantum information processor. *Physical Review Letters*, 107(16):160501, 10 2011. ISSN 0031-9007. URL <http://link.aps.org/doi/10.1103/PhysRevLett.107.160501>.
- [16] N.H. Nickerson, Y. Li, and S.C. Benjamin. Topological quantum computing with a very noisy network and local error rates approaching one percent. *Nature communications*, 4:1756, 1 2013. ISSN 2041-1723. URL <http://www.ncbi.nlm.nih.gov/pmc/articles/PMC3644110/>&tool=pmcentrez&rendertype=abstract.
- [17] M.A. Nielsen and I.L. Chuang. *Quantum Computation and Quantum Information*. Cambridge University Press, 2010.
- [18] W. Pfaff, T. H. Taminiau, L. Robledo, H. Bernien, M. Markham, D. J. Twitchen, and R. Hanson. Demonstration of entanglement-by-measurement of solid-state qubits. *Nature Physics*, 9(1):29–33, 10 2012. ISSN 1745-2473. URL <http://www.nature.com/doifinder/10.1038/nphys2444>.
- [19] W. Pfaff, B. Hensen, H. Bernien, S. B. van Dam, M. S. Blok, T. H. Taminiau, M. J. Tiggelman, R. N. Schouten, M. Markham, D. J. Twitchen, and R. Hanson. Unconditional quantum teleportation between distant solid-state quantum bits. *Science*, 332, 5 2014. ISSN 0036-8075. URL <http://www.science.org/cgi/doi/10.1126/science.1253512>.
- [20] M. D. Reed, L. DiCarlo, S.E. Nigg, L. Sun, L. Frunzio, S.M. Girvin, and R.J. Schoelkopf. Realization of three-qubit quantum error correction with superconducting circuits. *Nature*, 482(7385):382–5, 2 2012. ISSN 1476-4687. URL <http://www.ncbi.nlm.nih.gov/pubmed/22297844>.
- [21] L. Robledo, L. Childress, H. Bernien, B. Hensen, P.F.A. Alkemade, and R. Hanson. High-fidelity projective read-out of a solid-state spin quantum register. *Nature*, 477(7366):574–8, 9 2011. ISSN 1476-4687. URL <http://www.ncbi.nlm.nih.gov/pubmed/21937989>.
- [22] P. Schindler, J.T. Barreiro, T. Monz, V. Nebendahl, D. Nigg, M. Chwalla, M. Hennrich, and R. Blatt. Experimental repetitive quantum error correction. *Science (New York, N.Y.)*, 332(6033):1059–61, 5 2011. ISSN 1095-9203. URL <http://www.ncbi.nlm.nih.gov/pubmed/21617070>.
- [23] P.W. Shor. Algorithms for quantum computation: discrete logarithms and factoring. In *Proceedings 35th Annual Symposium on Foundations of Computer Science*, pages 124–134. IEEE Comput. Soc. Press, 1994. ISBN 0-8186-6580-7. URL <http://ieeexplore.ieee.org/lpdocs/epic03/wrapper.htm?arnumber=365700>.
- [24] B. Smeltzer, L. Childress, and A. Gali. ¹³C hyperfine interactions in the nitrogen-vacancy centre in diamond. *New Journal of Physics*, 13(2):025021, 2 2011. ISSN 1367-2630. URL <http://stacks.iop.org/1367-2630/13/i=2/a=025021?key=crossref.bdd6956722cde89a36ab3eee44a82724>.
- [25] T. H. Taminiau, J.J.T. Wagenaar, T. van der Sar, F. Jelezko, V.V. Dobrovitski, and R. Hanson. Detection and control of individual nuclear spins using a weakly coupled electron spin. *Physical Review Letters*, 109(13):137602, 9 2012. ISSN 0031-9007. URL <http://link.aps.org/doi/10.1103/PhysRevLett.109.137602><http://arxiv.org/abs/1205.4128>.
- [26] T. H. Taminiau, J. Cramer, T. van der Sar, V. V. Dobrovitski, and R. Hanson. Universal control and error correction in multi-qubit spin registers in diamond. *Nature Nanotechnology*, 2(February):2–7, 9 2014. ISSN 1748-3387. URL <http://arxiv.org/abs/1309.5452><http://www.ncbi.nlm.nih.gov/doifinder/10.1038/nnano.2014.2>.

- [27] T. van der Sar, Z.H. Wang, M.S. Blok, H. Bernien, T.H. Taminiau, D.M. Toyli, D.A. Lidar, D.D. Awschalom, R. Hanson, and V.V. Dobrovitski. Decoherence-protected quantum gates for a hybrid solid-state spin register. *Nature*, 484(7392):82–6, 4 2012. ISSN 1476-4687. URL <http://www.ncbi.nlm.nih.gov/pubmed/22481361>.
- [28] L.M. Vandersypen, M. Steffen, G. Breyta, C.S. Yannoni, M.H. Sherwood, and I.L. Chuang. Experimental realization of shor’s quantum factoring algorithm using nuclear magnetic resonance. *Nature*, 414(6866):883–7, 2001. ISSN 0028-0836. URL <http://www.ncbi.nlm.nih.gov/pubmed/11780055>.
- [29] G. Waldherr, Y. Wang, S. Zaiser, M. Jamali, T. Schulte-Herbrgggen, H. Abe, T. Ohshima, J. Isoya, J. F. Du, P. Neumann, and J. Wrachtrup. Quantum error correction in a solid-state hybrid spin register. *Nature*, 1 2014. ISSN 0028-0836. URL <http://arxiv.org/abs/1309.6424> <http://www.nature.com/doifinder/10.1038/nature12919>.

A

Dynamical Decoupling Spectroscopy

A.1 Mathematical description of dynamical decoupling spectroscopy

The observed signal due to the interaction between the NV-center and a single carbon in a dynamical decoupling spectroscopy experiment is given by Eqs. (A.1) to (A.4) [25]. Where P_x is the probability that the initial spin-state is preserved and M_j the contrast.

$$P_x = (M + 1)/2 \quad (\text{A.1})$$

$$M_j = 1 - (1 - \hat{\mathbf{n}}_0 \cdot \hat{\mathbf{n}}_1) \sin^2 \frac{N\phi}{2} \quad (\text{A.2})$$

$$1 - \hat{\mathbf{n}}_0 \cdot \hat{\mathbf{n}}_1 = \frac{A_\perp^2}{\tilde{\omega}^2} \frac{(1 - \cos(\tilde{\omega}\tau))(1 - \cos(\omega_L\tau))}{1 + \cos(\tilde{\omega}\tau)\cos(\omega_L\tau) - \left(\frac{A_\parallel + \omega_L}{\tilde{\omega}}\right) \sin(\tilde{\omega}\tau)\sin(\omega_L\tau)} \quad (\text{A.3})$$

$$\phi = \cos^{-1} \left(\cos(\tilde{\omega}\tau)\cos(\omega_L\tau) - \left(\frac{A_\parallel + \omega_L}{\tilde{\omega}}\right) \sin(\tilde{\omega}\tau)\sin(\omega_L\tau) \right) \quad (\text{A.4})$$

The contrast due to an ensemble of spins in a dynamical decoupling spectroscopy M is given by the product of all individual values M_j for each individual spin j (Eq. (A.5)).

$$M = \prod_j M_j \quad (\text{A.5})$$

A.2 Fingerprint analysis

The estimated hyperfine parameters of all 13 identified spins can be found in Table A.1. Due to the size of the fingerprint analysis it is not possible to include with this thesis. A pdf file containing the fingerprint analysis can be found here: <https://www.dropbox.com/s/gieji9e86bfvsf1/fingerprinting.pdf>.

Table A.1 – Estimated hyperfine parameters for spins 1 to 13.

Carbon	A_{\parallel}	A_{\perp}
1	$2\pi \cdot 30.0$ kHz	$2\pi \cdot 80.0$ kHz
2	$2\pi \cdot 27.0$ kHz	$2\pi \cdot 28.5$ kHz
3	$2\pi \cdot -51.0$ kHz	$2\pi \cdot 105.0$ kHz
4	$2\pi \cdot 45.1$ kHz	$2\pi \cdot 20.0$ kHz
5	$2\pi \cdot 17.0$ kHz	$2\pi \cdot 10.0$ kHz
6	$2\pi \cdot -15.0$ kHz	$2\pi \cdot 12.0$ kHz
7	$2\pi \cdot -23.0$ kHz	$2\pi \cdot 12.0$ kHz
8	$2\pi \cdot 10.0$ kHz	$2\pi \cdot 8.0$ kHz
9	$2\pi \cdot 8.0$ kHz	$2\pi \cdot 12.0$ kHz
10	$2\pi \cdot -9.3$ kHz	$2\pi \cdot 13.0$ kHz
11	$2\pi \cdot -10.0$ kHz	$2\pi \cdot 5.0$ kHz
12	$2\pi \cdot -30.0$ kHz	$2\pi \cdot 35.0$ kHz
13	$2\pi \cdot -32.0$ kHz	$2\pi \cdot 20.0$ kHz

B

Constants and Experimental values

Constants	
μ_0	$4\pi \cdot 10^{-7} \frac{\text{V}\cdot\text{s}}{\text{A}\cdot\text{m}}$
Gyromagnetic Ratios	
γ_e	$2\pi \cdot 2.8025 \text{ MHz/G}$
γ_N	$2\pi \cdot 0.3077 \text{ kHz/G}$
γ_C	$2\pi \cdot 1.0705 \text{ kHz/G}$
Interaction Strengths	
Δ	$2\pi \cdot 2.878 \text{ GHz}$
Q	$2\pi \cdot 4.946 \text{ MHz}$
A_N	$2\pi \cdot 2.186 \text{ MHz}$